Impact of Precursor Thermal Decomposition Reactions on YSZ Coatings Deposited with a Low-Power Plasma Torch at Short Spray Distance

Sandra Segondy, Catherine Rio, Stéphane Landais, Marie-Pierre Bacos, Cédric Guyon, Frédéric Rousseau

Impact of Precursor Thermal Decomposition Reactions on YSZ Coatings Deposited with a Low-Power Plasma Torch at Short Spray Distance

S. Segondy[1] · C. Rio[2] · S. Landais[2] · M.-P. Bacos[3] · C. Guyon[1] · F. Rousseau[1]

Abstract Yttria-stabilized zirconia (YSZ) deposition at short spray distance is of great interest for the aeronautic industry, especially to perform a thermal barrier coating (TBC) local repair. Typical thermal spray techniques usually employed to deposit such coatings are not designed for this type of application due to the powers involved. This work focuses on a plasma torch operating at atmospheric pressure, at low power (< 1 kW) and at short spray distance (4 mm). Precursor solutions are directly injected in the plasma afterglow to be sprayed and deposited onto a substrate. During flight time, precursor conversion is initiated. However, because of the low afterglow temperature (600 °C), droplets are not fully converted into YSZ when they impact the substrate. Typically, posttreatment is applied to improve the conversion of precursors into oxides, but this operation is very time- and therefore money-consuming. This study is focused on exploring a way to maximize the heat transfer to droplets already deposited by generating exothermicity using a redox reaction between zirconium and yttrium nitrates with ammonium acetate. This work highlights how exothermic precursor decomposition reactions as well as the gel-like consistency of the deposited clusters can improve both chemical conversion and coating microstructure.

Keywords atmospheric low-power plasma torch · solution precursor spraying · TBC · YSZ

This article is an invited paper selected from presentations at the 2022 International Thermal Spray Conference, held May 4–6, 2022 in Vienna, Austria, and has been expanded from the original presentation. The issue was organized by André McDonald, University of Alberta (Lead Editor); Yuk-Chiu Lau, General Electric Power; Fardad Azarmi, North Dakota State University; Filofteia-Laura Toma, Fraunhofer Institute for Material and Beam Technology; Heli Koivuluoto, Tampere University; Jan Cizek, Institute of Plasma Physics, Czech Academy of Sciences; Emine Bakan, Forschungszentrum Jülich GmbH; Šárka Houdková, University of West Bohemia; and Hua Li, Ningbo Institute of Materials Technology and Engineering, CAS.

✉ S. Segondy
sandra.segondy@chimieparistech.psl.eu

F. Rousseau
frederic.rousseau@chimieparistech.psl.eu

[1] Chimie ParisTech, PSL Research University, CNRS, Institut de Recherche de Chimie Paris (IRCP), 11 Rue Pierre Et Marie Curie, 75005 Paris, France

[2] ONERA, DMAS, Université Paris-Saclay, 92322 Châtillon Cedex, France

[3] Bacos Rhino Research Technology, 92160 Antony, France

Introduction

Combustion engines, such as turbojets, are built with nickel-based superalloys that are very resistant to deformation. However, given the high temperatures, mechanical stresses and oxidizing atmospheres that superalloys are exposed to, a thermal barrier coating (TBC) is required to ensure proper operation over a longer period of time (Ref 1, 2). TBCs are composed of an alumina-forming metallic bond coat (usually NiCrAlY), which promotes adherence and ensures better corrosion resistance of the substrate, and a ceramic coating (generally yttria-stabilized zirconia (YSZ)), which is a thermal insulator (Ref 3).

The ceramic coating is generally deposited by atmospheric plasma spray (APS) for the non-moving parts of the turbojet, such as the combustion chamber, and by electron beam physical vapor deposition (EBPVD) for the rotating parts, such as the turbine blades (Ref 4, 5). These two techniques result in two different coating morphologies:

columnar for EBPVD coatings and lamellar for APS coatings (Ref 3, 6). Columnar coatings have a slightly higher thermal diffusivity (4×10^{-7} m^2/s at 1100 °C (Ref 7)) than lamellar coatings but are more resistant to mechanical stress due to column presence, which is required for rotating parts. Lamellar coatings promote better thermal insulation, represented by a lower thermal diffusivity (2.3×10^{-7} m^2/s at 1100 °C (Ref 8)). The turbojet's combustion chamber is the most exposed to high temperatures due to fuel combustion; as such, good thermal insulation is essential (Ref 4, 5).

TBCs exposed to difficult environments can damage (cracks, delamination, etc.) requiring repairs. Generally, repair work involves a two-step process: TBC removal (by sandblasting or a high-pressure water jet, for example (Ref 9, 10)) followed by the entire TBC redeposition (usually with the same deposition techniques depending on the component type: APS, EBPVD). This process implies engine immobilization and turbojet disassembly and reassembly after the repair. This process is time-consuming and not very cost-effective, which is why local repair of the ceramic coating is of interest. Moreover, given the size, component geometry, accessibility and thermal spray process specificities (stand-off distance ranging between 50 and 150 mm (Ref 11, 12)), local repair of combustion chamber parts with commonly used plasma spray processes is impossible. To repair a combustion chamber locally, the plasma process developed needs to be equipped with a relatively small plasma torch that could operate close to the substrate.

Our work consists in developing a YSZ deposition technique functioning at low power (< 1 kW), at atmospheric pressure and at a short spray distance of 4 mm. Because low power is involved, the temperature in the afterglow reaches 600 °C which is too low to melt oxide particles (Ref 13) (ZrO_2 melting point: 2677 °C (Ref 14)). That is why precursor solutions are preferred, similarly to what is used in solution precursor plasma spray (SPPS). In our case, it implies that the only way to get "splat" or "granule" formation is to oxidize the precursors after they have reached the substrate under a liquid or a gel form. In previous works (Ref 13, 15), we highlighted that heat transfer is important to reach good precursor conversion values.

This work's aim is to explore ways to improve the conversion of precursors into YSZ and the microstructure obtained from water-based solutions by boosting the precursor thermal decomposition during the coating process (Ref 13). It involves testing strategies maximizing heat transfer to droplets already deposited. The goal is to obtain a morphology similar to that produced by APS (lamellar microstructure). Consequently, this study focuses on understanding the impact of precursor thermal decomposition reactions and more precisely their capacity to absorb or release heat (endo or exothermic processes). Typically, the strategy is to add a posttreatment step to the deposition process to help complete the decomposition of particles already deposited (Ref 13, 16, 17). The strategy presented hereafter consists of adding a reducing agent (acetate group in the form of ammonium acetate) to the solution (the zirconium and yttrium nitrate groups being the oxidizer) to produce an exothermic redox reaction as it was proposed by Muoto et al. (Ref 18, 19).

Experimental Procedure

Precursor Solution Preparation

Three different precursor solutions were produced, and the respective concentrations are presented in Table 1. The first solution did not include a reducer and was only composed of zirconium oxynitrate hydrate $ZrO(NO_3)_2{\cdot}6H_2O$, abbreviated to ZrO[n] (Sigma-Aldrich, USA) and yttrium nitrate hexahydrate $Y(NO_3)_3{\cdot}6H_2O$, abbreviated to Y[n] (Sigma-Aldrich, USA). Ammonium acetate CH_3COONH_4, abbreviated to NH_4[a] (Sigma-Aldrich, USA), was added to the other two solutions. In the second solution (ZrO[n]Y[n] + 50% NH_4[a]), 50 mol% ammonium acetate of the total molar quantity of nitrates in solution was added. The third solution (ZrO[n]Y[n] + 100% NH_4[a]) contained 100 mol% of ammonium acetate in addition to the nitrate mixture. Net oxidizing and reducing valencies were calculated for each reactant by adding the net valencies of every atom (Ref 19, 20). The valencies of oxygen, nitrogen, hydrogen, yttrium, carbon and zirconium were considered equal to 2 −, 0, 1 +, 3 +, 4 + and 4 +, respectively. The net valencies of zirconium oxynitrate, yttrium nitrate and ammonium acetate were therefore 10 −/mol, 15 −/mol and 11 + /mol, respectively. In the case of a 92/8 mol% ratio between $ZrO(NO_3)_2$ and $Y(NO_3)_3$, the net valency was 10.4 −/mol. Therefore, in regard to valencies to balance the redox reaction, the reducing agent was added in a slight excess, as the ratios between reducers (NH_4[a]) and oxidizers (ZrO[n]Y[n]) corresponded to 52.9 mol% and 105.8 mol%. For each solution, the reactants were dissolved and mixed in deionized water (ZrO[n]Y[n] concentration: 0.05 M) to obtain a final composition of 7.4 wt% Y_2O_3-ZrO_2.

Solution Characterization

Each solution was evaporated to analyze its thermal behavior by differential scanning calorimetry (DSC). Solutions were evaporated on a heating plate (programmed at 230 °C in order to reach 100 °C in the beaker) until the

Table 1 Composition of the solutions produced

	Molar concentration, mol/L			Mass concentration, g/L		
	ZrO[n]	Y[n]	NH_4[a]	ZrO[n]	Y[n]	NH_4[a]
ZrO[n]Y[n]	4.25×10^{-2}	3.70×10^{-3}	0	14.4	1.4	0
ZrO[n]Y[n] + 50 mol% NH_4[a]	4.25×10^{-2}	3.70×10^{-3}	2.31×10^{-2}	14.4	1.4	1.8
ZrO[n]Y[n] + 100 mol% NH_4[a]	4.25×10^{-2}	3.70×10^{-3}	4.62×10^{-2}	14.4	1.4	3.6

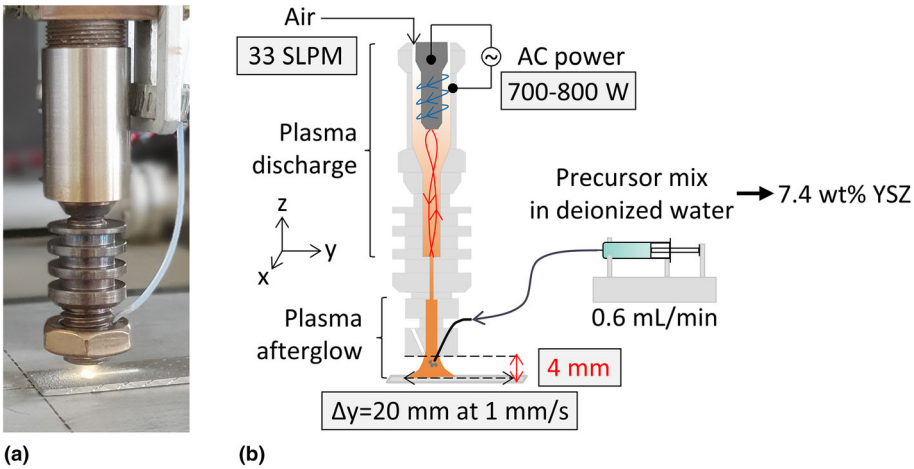

Fig. 1 (a) Photograph of the plasma torch in operation (b) schematic of the experimental setup

reactants reached a dried gel-like consistency. The evaporation process took approximately one hour to be completed. Dried gel enthalpies of reaction (endo or exothermic) resulting from their decomposition were evaluated with a DSC instrument (DSC131 EVO, SETARAM Instrumentation, France). The analyses were performed by heating 53 ± 1 mg of each sample from 25 to 450 °C at 10 °C/min rate in aluminum crucibles.

Coating Deposition

The plasma torch used in this study was designed by AcXys Plasma Technologies (France), and its principle was described in a previous paper (Ref 13). The experimental setup is visible in Fig. 1. The plasma discharge was generated by AC electrical power with a typical frequency of 80 kHz between two electrodes. This process operated at a high gas flow rate of 33 SLPM, which pushed the plasma discharge beyond the electrodes and formed the plasma afterglow. Air was used as the discharge gas and plasma power ranged between 700 and 800 W. The temperature of the plasma afterglow was previously estimated at 600 °C (Ref 13). The coating scanning pattern followed multiple scans on the same single line across the substrate at a speed of 1 mm/s, which resulted in coating depositions covering approximately a 25 × 5 mm^2 surface area and maximizing heat transfer between the plasma afterglow and the substrate. The substrate, a superalloy substrate (Hastelloy-X), with a NiCrAlY bond coat (32 × 17 × 1.5 mm) was placed at a distance of 4 mm from the nozzle exit. Before deposition, the substrate was preheated by 6 scans (2 min) of the plasma torch to reach a temperature of around 200 or 250 °C, which promoted coating adhesion to the substrate.

An injector connected to a syringe pump (BIOSEB 8000/9000, France) was used to spray the precursors solution directly into the plasma afterglow at a liquid flow rate of 600 µL/min. It was positioned at 1 mm from the torch nozzle exit and was centered based on the afterglow. The total solution volume injected was fixed to 16 mL. Coatings were therefore obtained after 86 scans (6 scans of substrate preheating and 80 scans of deposition, 28min40s total).

In some cases, a posttreatment step was added to the deposition process. Posttreatment corresponded to a step where no additional precursor solution was injected. The plasma afterglow only treated the droplets that had been previously deposited onto the substrate's surface. The deposition cycle was as follows: precursor injection for one minute followed by one minute of posttreatment. This cycle was repeated 26 times to reach the targeted volume of precursor solution. Coatings with posttreatment were

obtained after 166 scans (55min20s total): 6 scans of substrate preheating, 80 scans of deposition and 80 scans of posttreatment. An annealing step corresponding to the first heating cycle of the engine was performed on some of the deposits (even for posttreated ones) to replicate the conditions of use. These samples were annealed at 1100 °C for 1 h in an open-air furnace (Pyrox Thermique Matériaux, France). The heating rate was set at 200 °C/h.

Coating Characterization

Fourier transformed infrared spectroscopy (FTIR) instrument (Agilent Technologies Cary 600 Series FTIR spectrometer, USA) equipped with a diamond ATR (PIKE Technologies GladiATR, USA) was used to assess the precursor conversion into oxides. Two bands were specifically tracked: the first one centered at around 1250 cm^{-1} corresponding to the stretching vibration of N–O from NO_3^- (visible when nitrates were remaining in the coating and coordinated to a metal) and the second peak at 400 cm^{-1} corresponding to the stretching vibration of Zr-O, both visible in the precursor ($ZrO(NO_3)_2$) and the oxide (ZrO_2), as described in a previous work (Ref 13). Precursor conversion to oxides was estimated by tracking the 1250 cm^{-1} band intensity, which was the most intense nitrate band, as well as the 400 cm^{-1} one. It is important to note that FTIR analyses were done at multiple locations on each coating and corresponded to the entire thickness. This allowed estimating an average composition. However, there could be conversion disparities between coating's top and bottom parts and the absorbance value was maybe not homogenous through the coating's thickness.

Coating crystallinity was analyzed through an x-ray diffractometer (Malvern PANalytical XPERT Pro, UK) to obtain XRD patterns and determine YSZ crystallographic phase (diffractograms ranging between 20° and 80° at a scan speed of 0.042°/s).

Cross-sectional morphologies were studied through scanning electron microscopy (TESCAN MIRA3, Czech Republic). Beforehand, the samples were embedded in an epoxy resin (Araldite, ESCIL, France), cut, and then ground with abrasive paper (gradation 350, 1200, 4000 for 5 min each) and polished with diamond suspensions on corresponding pads (6, 3, ¼ µm for 15, 5 and 5 min, respectively) on a manual grinding and polishing machine (Struers Planopol Polisher, Denmark). Coating porosity was assessed through image analysis with ImageJ software (free open-source software), by converting the image to black and white pixels depending on a manually set threshold. The ratio between black and white pixels represented the porosity of the image studied. To calculate the porosity, five images were analyzed three times for each sample.

The first solidified droplets were studied by SEM (Quattro S, Thermo Fisher Scientific, USA) to compare their structure depending on the precursor type. Two scans were performed on the same line on stainless steel instead of superalloy to facilitate droplet localization. The substrate was first preheated by multiple scans of the plasma torch. Before every SEM analysis, a metallic coating was sprayed on top of the sample (Cressington sputter coater 108 under argon, Germany).

Results and Discussion

Study of Precursor Thermal Decomposition Reactions

For all solutions, a dried gel consistency is obtained as shown in Fig. 2(a)-(c). It is important to note that both solutions containing a nitrate/acetate mixture showed a gel precipitation halfway through the evaporation process. Also, the dried gels look different from the one with ZrO[n]Y[n] only. This correlates to the heterogenous gel formation observed by just mixing zirconium oxynitrate hydrate and ammonium acetate powders. This can be explained by the interaction between hydrated nitrate and hygroscopic ammonium acetate molecules. It is likely that counterions are swapped between zirconium nitrate and ammonium acetate leading to the formation of zirconium acetate, which forms a hydroxy-bridged polymer which is known to be a hydrophobic compound (Ref 21, 22).

DSC thermographs of these dried gels are presented in Fig. 3. The ZrO[n]Y[n] thermal decomposition is confirmed to be an overall endothermic process from 25 to 450 °C through the presence of three broad peaks at 143, 226 and 268°C of − 53, − 40 and − 39 mW, respectively. The first one starting at 100 °C can be associated with hydration water evaporation while the other can be correlated to reactions leading to zirconium and yttrium oxidation and nitrate decomposition. As expected, solutions containing a nitrate/acetate mix show two exothermic peaks for temperatures over 250 °C, which corresponds to combustion reactions correlated to precursor decomposition and metal oxidation (Ref 18, 19). For ZrO[n]Y[n] + 50 mol% NH_4[a], three peaks are visible, the first one at 158 °C is endothermic (− 34 mW) while the other two at 260 °C (+ 164 mW) and at 303 °C (+ 20 mW) are exothermic. For ZrO[n]Y[n] + 100 mol% NH_4[a], no endothermic trough is clearly visible, but two exothermic peaks at 270 °C (+ 244 mW) and at 334 °C (+ 69 mW) are noticeable. The produced exothermic heat reaches higher values when the acetate is more concentrated in the solution. This is expected because more reducer is available to react with the oxidizing agent

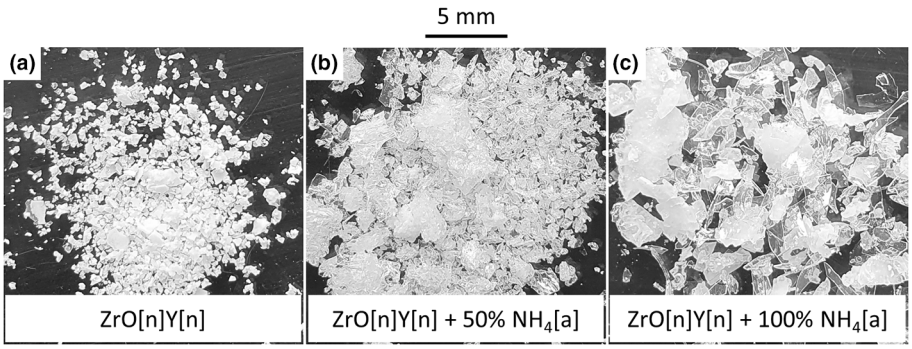

Fig. 2 Photographs of evaporated solutions (a) ZrO[n]Y[n], (b) ZrO[n]Y[n] + 50 mol% NH_4[a] and (c) ZrO[n]Y[n] + 100 mol% NH_4[a]

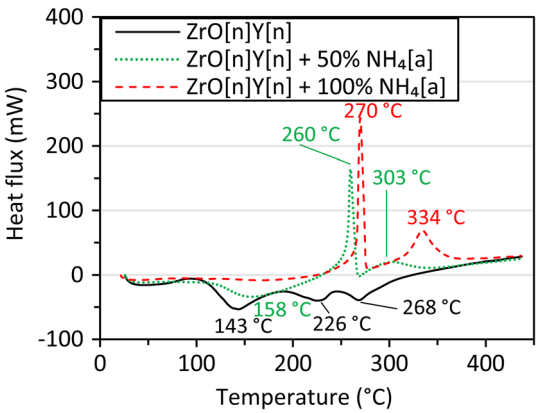

Fig. 3 DSC thermographs obtained from evaporated solutions

(nitrate molecules) leading to a more energetic combustion reaction. Thermal decomposition of nitrate and acetate groups coordinated to a metal leads to the formation of the corresponding oxide as well as secondary compounds, which are released as gases (such as NO_x or CO_2).

Study of First Droplets Deposited on the Surface

SEM images of the first droplets deposited on the substrate surface are presented in Fig. 4. As shown in images (a)-(c), granules have different sizes, ranging between less than 1 µm and above 5 µm for all solutions tested. Compared to what is obtained with SPPS, no large splats that would correspond to flatten spherical molten droplets are visible (Ref 23).The temperature is not high enough to melt the particles and therefore to produce such structures in our case. It is likely that the "clusters" are made of a mixture of remaining precursors and partly amorphous, partly crystallized 7.4YSZ if the thermal decomposition process is not complete.

Figure 4(d)-(f) is close-ups of the biggest granules deposited on the surface from solutions containing 0 mol, 50 mol and 100 mol% acetate, respectively. The cluster porosity difference is clearly visible on these three images. In the case of the solution ZrO[n]Y[n], the biggest particles exhibit a very porous morphology. The ones from solutions ZrO[n]Y[n] + 50 or 100 mol% NH_4[a] clearly show the gel-like consistency expected for a nitrate/acetate mix and porosities are less visible. The clusters' density depends on the reducer/oxidizer ratio. This implies that remaining precursors are composed of zirconium acetate and that the particles need to be further treated by multiple scans to boost the thermal decomposition/combustion process. Flight time is therefore too short to fully support precursor conversion

Precursor Conversion

As shown in the DSC analysis, nitrate thermal decomposition is exclusively an endothermic process. A typical way to tend toward a full precursor conversion is to increase the contact time between deposited droplets and the plasma afterglow by adding a posttreatment step to the coating process. Figure 5 compares FTIR spectra from coatings produced with and without a posttreatment step or with two different ammonium acetate amounts. When comparing spectra corresponding to coatings with and without a posttreatment step, we can see that a lower nitrate amount is remaining with a posttreatment step, as made evident by the low absorbance value at 1250 cm^{-1} corresponding to the N–O stretching band compared to the absorbance of Zr−O stretching vibration at 400 cm^{-1}. Peaks at 1020 and 1550 cm^{-1} are, respectively, associated with bands from the NO stretching and the asymmetric NO_3 stretching (Ref 24). This confirms that adding a posttreatment step to the coating cycle can improve the precursor conversion.

The nitrate conversion for precursor mixtures containing ammonium acetate reaches the same value as when a posttreatment step is added to the coating process. The N–O absorbance value for both ammonium acetate percentages is indeed equivalent to the posttreatment one. It means that increasing the heat available by generating an exothermic reaction is helping the conversion process just like a posttreatment does. The redox reaction is advantageous because the conversion is the same as with a posttreatment step, but it requires twice less time to form a coating.

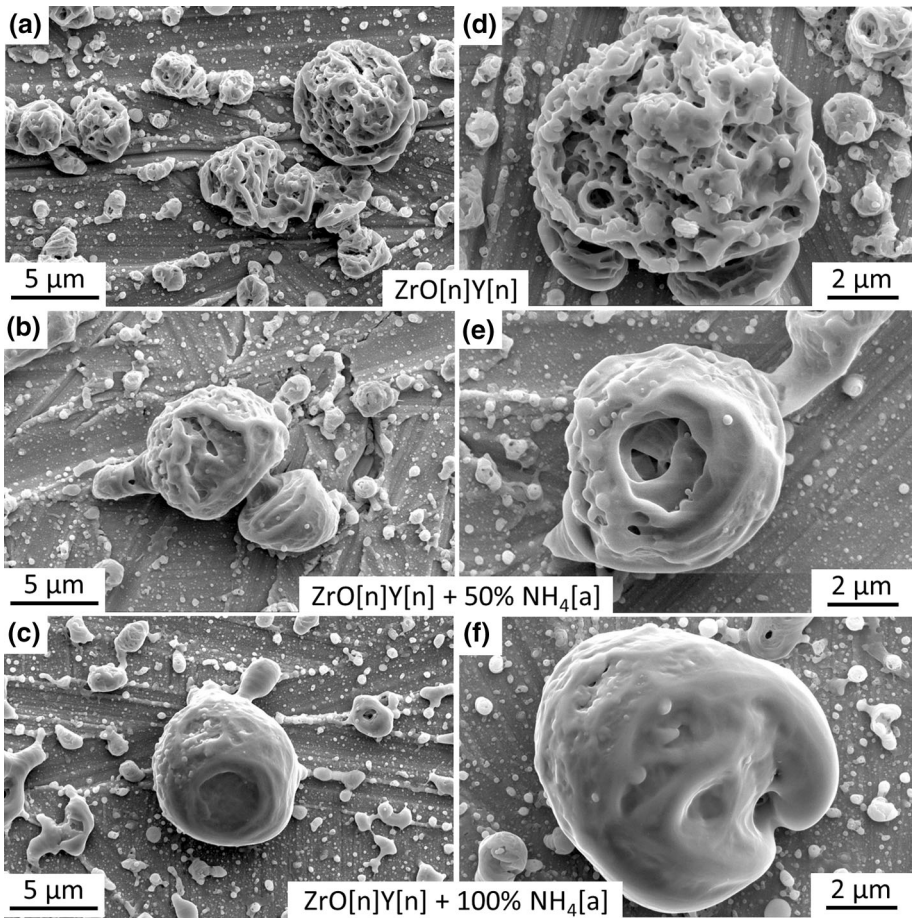

Fig. 4 SEM images of particles deposited after two scans at two different magnifications from solutions containing (a); (d) ZrO[n]Y[n] (b); (e) ZrO[n]Y[n] + 50 mol% NH_4[a] and (c); (f) ZrO[n]Y[n] + 100 mol% NH_4[a]

However, the band located at 1380 cm^{-1} is associated with the symmetric carboxylate band. The one at 1520 cm^{-1} is an overlap between the antisymmetric carboxylate band from the acetate and the asymmetric NO_3 stretching band from the nitrate (Ref 25). This implies that not all acetate groups are decomposed during the coating process. Adding 50 or 100 mol% of acetate does not seem to make any difference conversion-wise. Even if increasing the ammonium acetate amount is improving the exothermic reaction, it is also adding more precursors to decompose. That is maybe why the 100 mol% FTIR spectrum is the same as when only 50 mol% is added to the solution. These results confirm that giving more thermal energy to the coating can improve the conversion. Moreover, no large band between 2600 and 3600 cm^{-1} associated with O–H stretching vibrations is visible, meaning that all water molecules from the precursors and solution have been evaporated.

Coating Composition and Microstructures

Figure 6 illustrates coating cross-sectional SEM images deposited with solutions with or without a posttreatment as well as with or without ammonium acetate. The SEM images presented here correspond to deposits before annealing. When comparing pictures (a), (c) and (d) corresponding to coatings produced with solutions with 0 mol, 50 mol and 100 mol% acetate, respectively, differences in microstructure are visible. The coating made with the ZrO[n]Y[n] precursor solution, shown in Fig. 6(a), exhibits a columnar-like microstructure and is overall quite porous. Its porosity was evaluated at 30 ± 5%. Its microstructure was further discussed in (Ref 15). Figure 6(b) is illustrating a coating produced with the ZrO[n]Y[n] precursor solution but with a posttreatment step. The overall microstructure is considered denser than without a posttreatment (porosity of 28 ± 5%). However, there are still quite porous regions similar to what is observed in Fig. 6(a), especially close to the substrate. In the case of the coating produced with the solution made with ZrO[n]Y[n] + 50% NH_4[a] (Fig. 6c), it appears relatively denser (porosity of 27 ± 3%). There is

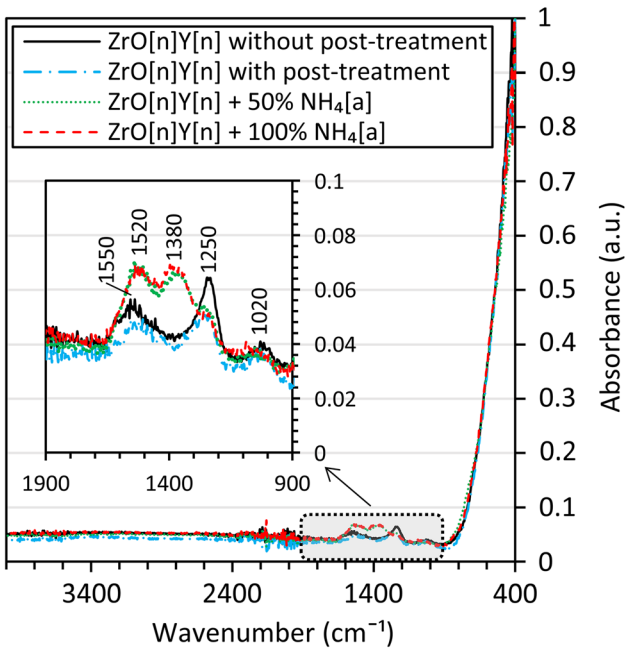

Fig. 5 FTIR spectra obtained for coatings produced from the solutions containing ZrO[n]Y[n] with and without a posttreatment step, ZrO[n]Y[n] + 50 mol% NH_4[a] and ZrO[n]Y[n] + 100 mol% NH_4[a]

a contrast between the top and the bottom parts. Close to the substrate, more porosities are visible, and the coating is like what is obtained with the nitrate-based solution. However, the coating's top part appears less porous and more homogenous. These differences are even sharper for the coating made with the solution containing 100 mol% of ammonium acetate, shown in Fig. 6(d). The bottom part is particularly porous and appears more columnar (porosity of 37 ± 7%). In contrast, the top part is showing very little porosities (porosity of 20 ± 4%). In some coating's regions, there are cracks parallel to the substrate splitting up the coating in two, as illustrated in the SEM picture. It appears that in all cases, the coating's microstructure is denser at the top than at the bottom. This phenomenon was already explained in (Ref 15) but it is shown here that it is valid for different precursor type and is not limited to water-based nitrate solutions.

As a reminder, for both nitrates and acetates, thermal decomposition implies releasing gases, such as NO_x or CO_2. As they are released from the coating, these gases can create bigger porosities, columnar structures, or cracks. That is why it is important to release them gradually while increasing the coating thickness. Adding 100 mol% of ammonium acetate to the nitrates forms a precursor solution that generates an important exothermic response during the thermal decomposition process. It means that the precursors are quickly converted and therefore release a large gas volume in a small amount of time. This phenomenon can explain the porosity formation as well as the coating delamination right at the center. Moreover, because the clusters deposited are denser with a higher oxidizer/reducer ratio, the gases can be entrapped by the overall top layer densification, leading to the coating delamination. When only 50 mol% of ammonium acetate is added to the solution, the microstructure is more stable. Because the conversion was evaluated equivalent by FTIR analysis, it means that a higher oxidizer/reducer ratio emphasizes the thermal decomposition process.

SEM pictures took from coating's regions close to the substrate at high magnification are presented in Fig. 6(e) to (h). These pictures illustrate microstructure differences. Figure 6(e) and (f) corresponds to coatings made with the ZrO[n]Y[n] precursor solution without or with a post-treatment, respectively. Nanoscale porosities are clearly visible, especially on the picture (e). These small porosities are almost completely gone in the case of precursor solutions including ammonium acetate (Fig. 6g and h). These differences can be linked to the first droplets microstructure as a function of the precursor type shown in the previous section. Because the intermediate compound formed (supposedly zirconium acetate) has a strong gel consistency, it helps getting a more compact microstructure. That is probably why the coating top part is particularly dense in Fig. 6(c) and (d).

The deposits were also observed after annealing. The clear difference observed at a microscopic scale between coatings produced using the nitrate-only solution with a posttreatment step and the ones made with nitrate/acetate solutions is still noticeable and not modified after annealing.

Coating Phase Composition

Figure 7 showcases diffractograms obtained for coatings displaying the best conversion according to FTIR analysis, before and after an annealing step at 1100 °C for one hour. The experimental conditions are: ZrO[n]Y[n] solution with a posttreatment step, ZrO[n]Y[n] + 50% NH_4[a] solution and ZrO[n]Y[n] + 100% NH_4[a] solution. As the deposited coating's thickness is approximately 130 µm, peaks corresponding to the substrate crystalline structure are visible and are indicated on the figure. XRD data obtained before the annealing step show that as-deposited coatings exhibit peaks coinciding to the expected YSZ tetragonal phase. However, the peaks are not all well-defined, especially for coatings deposited with a precursor solution containing ammonium acetate. As a reminder, FTIR analyses show that a certain precursor amount is remaining in the coating, which have an amorphous phase (see section precursor conversion). It is particularly true for coatings still including carbon-based compounds. That can explain

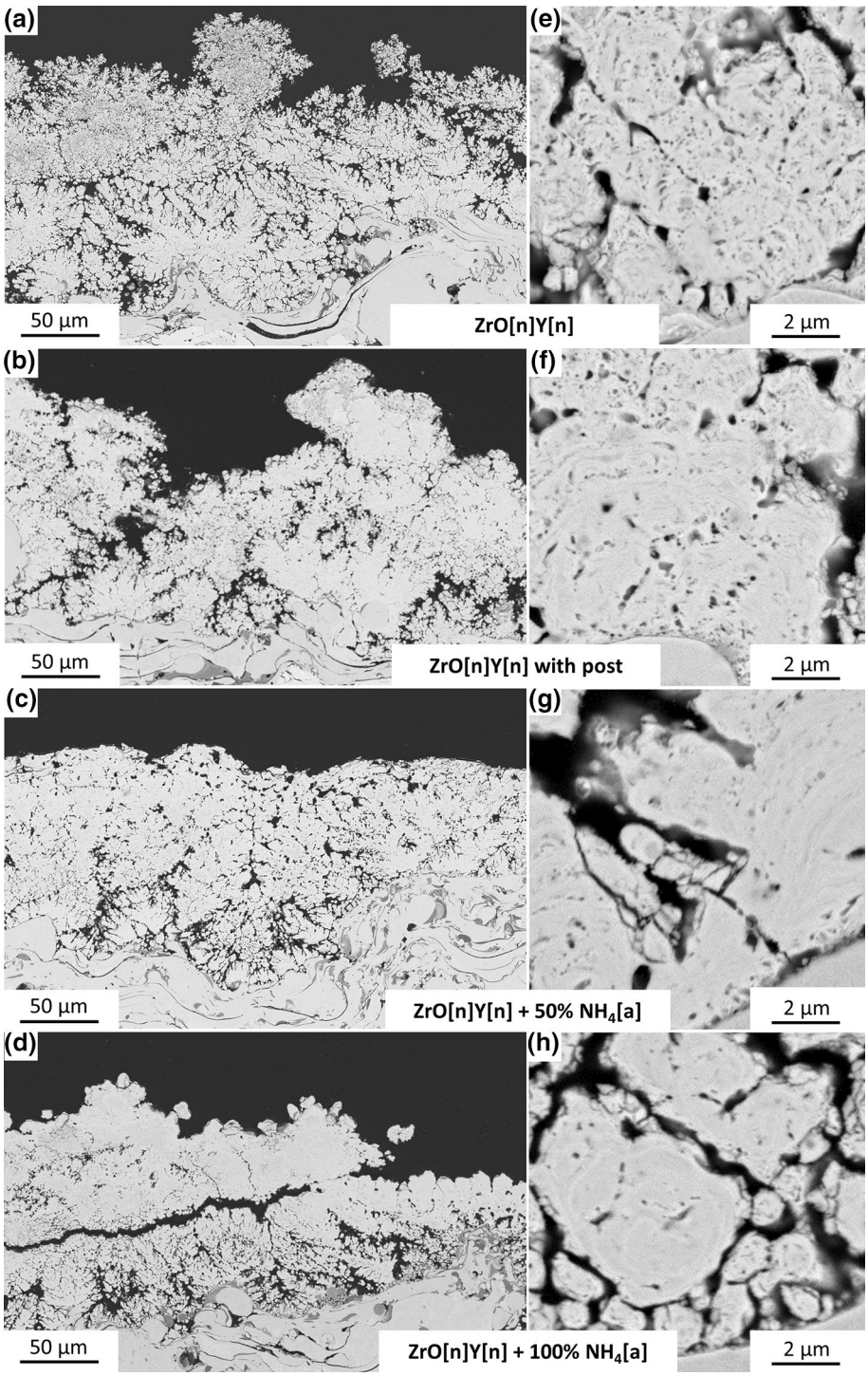

Fig. 6 Cross-sectional SEM images of coatings deposited by injecting solutions containing (a) ZrO[n]Y[n], (b) ZrO[n]Y[n] with posttreatment, (c) ZrO[n]Y[n] + 50% NH_4[a], (d) ZrO[n]Y[n] + 100% NH_4[a], (e), (f), (g) and (h) close-up SEM images in respective order

why peaks from both coatings produced with ammonium acetate in the solution have a weaker intensity compared to the one deposited with the ZrO[n]Y[n] precursor solution with a posttreatment. Diffractograms of coatings after annealing is shown in Fig. 7 as well. The peaks are more defined, demonstrating better crystallinity due to more elevated temperatures, and the pattern still only contains the peaks of the expected YSZ tetragonal phase. It is also

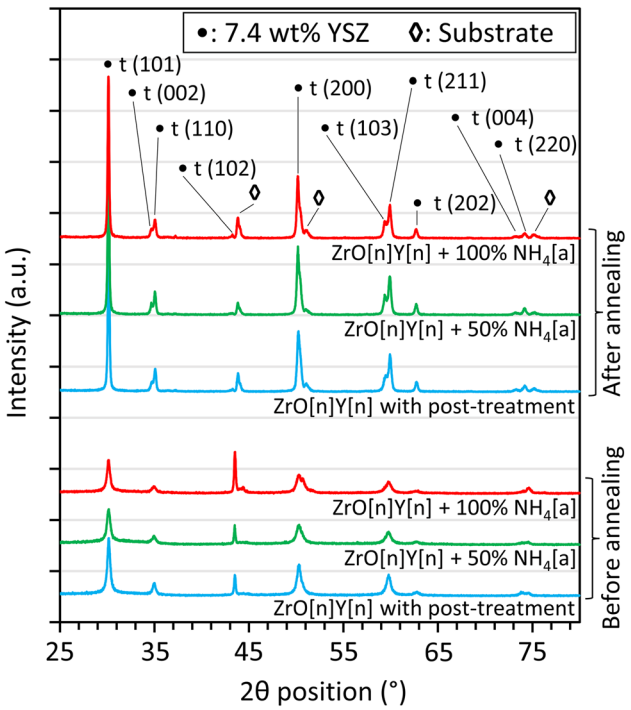

Fig. 7 XRD diffractograms obtained for coatings produced from solutions as indicated (before and after an annealing step at 1100 °C for one hour)

seen that whatever the precursor solution used, the diffractograms obtained after the annealing step are all identical. It means that when the coating reaches higher temperatures, the precursor type employed to make the solution does not affect the coating's crystalline structure.

Conclusion and Perspectives

A YSZ deposition operated at atmospheric pressure, low power of 700–800 W and short spray distance of 4 mm involved specific operating conditions at temperature less than 800 °C, different than the ones employed in thermal spray techniques such as SPPS or APS. Compared to these methods, the phenomenon was different because precursors in solution cannot be converted into oxides and melted before their impact with the substrate as with thermal plasma. That is why maximizing heat transfer to droplets already deposited was crucial in a process like the one presented in this work. YSZ coatings were produced by injecting a water-based precursor solution directly in the plasma afterglow. All solutions were at least composed of a zirconium oxynitrate and yttrium nitrate mixture. The ratio was chosen so that the final composition of the coatings was 7.4 wt% Y_2O_3-ZrO_2. As it was confirmed by DSC analyses, nitrate groups underwent endothermic thermal decomposition when exposed to heat, meaning that they required energy to go through their reaction process. Adding a posttreatment increased the contact time between deposited droplets and the plasma afterglow resulting in a conversion improvement due to the temperature as well as the presence of oxidative species in the plasma afterglow. Concerning the microstructure, the posttreatment step did reduce slightly the porosity value. However, this approach also multiplied by two the experiment time, which is not ideal. Ammonium acetate was added with a specific molar ratio in some solutions. Interestingly, nitrate and acetate together caused redox reactions, making the process exothermic. The release of heat during the decomposition generated enough energy to improve the precursor conversion. FTIR analyses showed that the conversion was indeed improved with acetate added to the mix. SEM pictures illustrated interesting microstructures. For 50 or 100 mol% of ammonium acetate added to the solution, the particles (granules) appeared denser at a microscale. This can explain why the microstructure was more homogenous with the ZrO[n]Y[n] + 50% NH_4[a] solution. It is, however, important to manage the exothermic reaction. In the case of the ZrO[n]Y[n] + 100% NH_4[a] solution, the reaction was supposedly too powerful and the coating was getting too dense entrapping the gases formed, leading to the coating delamination at the center.

Even though working with a reducer/oxidizer mixture improved the thermal decomposition, a full conversion was still not reached. This implies that a small number of carbon-based compounds were remaining in the coating at the end. Also, the XRD analysis showed that the coatings were more amorphous when produced with solutions containing ammonium acetate. However, after an annealing step at 1100 °C, all diffractograms were equal, corresponding to the expected YSZ tetragonal phase. These results showcased how the precursor conversion and coating microstructure can be improved through exothermic thermal decomposition reactions.

Author Contributions SS contributed to conceptualization, investigation, writing–original draft preparation, writing–reviewing and editing, CR contributed to investigation, SL contributed to conceptualization, methodology, investigation, M-PB contributed to conceptualization, methodology, investigation, writing–original draft preparation, writing–reviewing and editing, CG contributed to conceptualization, methodology, investigation, supervision, writing–reviewing and editing, and FR contributed to conceptualization, methodology, investigation, supervision, writing–original draft preparation, writing–reviewing and editing, project administration, funding acquisition.

References

1. W. Beele, G. Marijnissen, and A. van Lieshout, The Evolution of Thermal Barrier Coatings — Status and Upcoming Solutions for Today's Key Issues, *Surf. Coat. Technol.*, 1999, **120-121**, p 61–67.
2. B. Gleeson, Thermal Barrier Coatings for Aeroengine Applications, *Journal of Propulsion and Power, American Institute of Aeronautics and Astronautics*, 2006, **22**(2), p 375–383.
3. S. Bose, Chapter 7 - Thermal Barrier Coatings (TBCs), *High Temperature Coatings (Second Edition)*, S. Bose, Ed, Butterworth-Heinemann, 2018, p 199–299, https://doi.org/10.1016/B978-0-12-804622-7.00007-3.
4. C.U. Hardwicke and Y.-C. Lau, Advances in Thermal Spray Coatings for Gas Turbines and Energy Generation: A Review, *J. Therm. Spray Technol.*, 2013, **22**(5), p 564–576.
5. A. Feuerstein, J. Knapp, T. Taylor, A. Ashary, A. Bolcavage, and N. Hitchman, Technical and Economical Aspects of Current Thermal Barrier Coating Systems for Gas Turbine Engines by Thermal Spray and EBPVD: A Review, *J Therm Spray Tech*, 2008, **17**(2), p 199–213.
6. M. Karger, R. Vaßen, and D. Stöver, Atmospheric Plasma Sprayed Thermal Barrier Coatings with High Segmentation Crack Densities: Spraying Process, *Microstructure and Thermal Cycling Behavior, Surface and Coatings Technology*, 2011, **206**(1), p 16–23.
7. B.-K. Jang and H. Matsubara, Thermophysical Properties of EB-PVD Coatings and Sintered Ceramics of 4mol% Y2O3-Stabilized Zirconia, *J. Alloy. Compd.*, 2006, **419**(1), p 243–246.
8. H. Wang, R.B. Dinwiddie. and W.D. Porter, Development of a Thermal Transport Database for Air Plasma Sprayed ZrO2-Y2O3 Thermal Barrier Coatings, *J Therm Spray Tech*, 2010, **19**(5), p 879–883.
9. J.M. Sohr and M.L. Thorpe, Stripping of Thermal Spray Coatings with Ultra High Pressure Water Jet, *SAE Transactions, SAE International*, 1992, **101**, p 51–59.
10. M. Anguelo and G. Angulo, "Stripper Assembly for Combustion Chambers of Turbine or Jet Engines," 1991, https://patents.google.com/patent/US5018320/en. Accessed 14 April 2020.
11. F. Chang, K. Zhou, X. Tong, L. Xu, X. Zhang. and M. Liu, Microstructure and Thermal Shock Resistance of the Peg-Nail Structured TBCs Treated by Selective Laser Modification, *Appl. Surf. Sci.*, 2014, **317**, p 598–606.
12. S. Tao, J. Yang, W. Li, F. Shao, X. Zhong, H. Zhao, Y. Zhuang, J. Ni, S. Tao. and K. Yang, Thermal Stability of Plasma-Sprayed Thick Thermal Barrier Coatings Using Triplex ProTM-200 Torch, *Coatings, Multidisciplin Dig Publish Institute*, 2020, **10**(9), p 894.
13. S. Segondy, C. Rio, S. Landais, C. Guyon, and F. Rousseau, "Development of a Low Power Plasma Reactor for the Local Deposition of YSZ Thermal Barrier Coatings at Atmospheric Pressure," ASM International, 2022, p 447–452, https://doi.org/10.31399/asm.cp.itsc2022p0447.
14. H. Xiong and W. Sun, Investigation of Droplet Atomization and Evaporation in Solution Precursor Plasma Spray Coating, *Coatings*, 2017, **7**(11), p 207.
15. S. Segondy, "Dépôt Local de Zircone Yttriée Par Plasma Atmosphérique Basse Puissance: Applications Aux Turbines Aéronautiques (Available Online in November 2022)," Université Paris sciences et lettres, 2022, https://www.theses.fr/s275675. Accessed 6 October 2022.
16. F. Rousseau, C. Fourmond, F. Prima, M.H. Vidal Serif, O. Lavigne, D. Morvan. and P. Chereau, Deposition of Thick and 50% Porous YpSZ Layer by Spraying Nitrate Solution in a Low Pressure Plasma Reactor, *Surf. Coat. Technol.*, 2011, **206**(7), p 1621–1627.
17. F. Rousseau, A. Quinsac, D. Morvan, M.-P. Bacos, O. Lavigne, C. Rio, C. Guinard. and B. Chevillard, A New Injection System for Spraying Liquid Nitrates in a Low Power Plasma Reactor: Application to Local Repair of Damaged Thermal Barrier Coating, *Surf. Coat. Technol.*, 2019, **357**, p 195–203.
18. C.K. Muoto, E.H. Jordan, M. Gell. and M. Aindow, Identification of Desirable Precursor Properties for Solution Precursor Plasma Spray, *J Therm Spray Tech*, 2011, **20**(4), p 802–816.
19. C.K. Muoto, E.H. Jordan, M. Gell. and M. Aindow, Phase Homogeneity in Y2O3–MgO Nanocomposites Synthesized by Thermal Decomposition of Nitrate Precursors with Ammonium Acetate Additions, *J. Am. Ceram. Soc.*, 2011, **94**(12), p 4207–4217.
20. S.R. Nair, R.D. Purohit, P.K. Sinha. and A.K. Tyagi, Sr-Doped LaCoO3 through Acetate-Nitrate Combustion: Effect of Extra Oxidant NH4NO3, *J. Alloy. Compd.*, 2009, **477**(1–2), p 644–647.
21. A.C. Geiculescu and H.G. Spencer, Thermal Decomposition and Crystallization of Aqueous Sol-Gel Derived Zirconium Acetate Gels: Effects of the Additive Anions, *J. Sol-Gel. Sci. Technol.*, 2000, **17**(1), p 25–35.
22. S. Deville, C. Viazzi. and C. Guizard, Ice-Structuring Mechanism for Zirconium Acetate, *Langmuir*, 2012, **28**(42), p 14892–14898.
23. A. Joulia, G. Bolelli, E. Gualtieri, L. Lusvarghi, S. Valeri, M. Vardelle, S. Rossignol. and A. Vardelle, Comparing the Deposition Mechanisms in Suspension Plasma Spray (SPS) and Solution Precursor Plasma Spray (SPPS) Deposition of Yttria-Stabilised Zirconia (YSZ), *J. Eur. Ceram. Soc.*, 2014, **34**(15), p 3925–3940.
24. B.M. Gatehouse, S.E. Livingstone. and R.S. Nyholm, Infrared Spectra of Some Nitrato and Other Oxy-Anion Co-Ordination Complexes, *J. Inorg. Nucl. Chem.*, 1958, **8**, p 75–78.
25. J.E. Tackett, FT-IR Characterization of Metal Acetates in Aqueous Solution Appl Spectrosc, AS, *Soc. Appl. Spectroscopy*, 1989, **43**(3), p 483–489.